Photodynamic Therapy Hot Paper

How to cite:
International Edition: doi.org/10.1002/anie.202106748
German Edition: doi.org/10.1002/ange.202106748

BODIPY-Based Photodynamic Agents for Exclusively Generating Superoxide Radical over Singlet Oxygen

Kun-Xu Teng[+], Wen-Kai Chen[+], Li-Ya Niu, Wei-Hai Fang, Ganglong Cui, and Qing-Zheng Yang**

Abstract: *Developing Type-I photosensitizers is considered as an efficient approach to overcome the deficiency of traditional photodynamic therapy (PDT) for hypoxic tumors. However, it remains a challenge to design photosensitizers for generating reactive oxygen species by the Type-I process. Herein, we report a series of α,β-linked BODIPY dimers and a trimer that exclusively generate superoxide radical ($O_2^{-\bullet}$) by the Type-I process upon light irradiation. The triplet formation originates from an effective excited-state relaxation from the initially populated singlet (S_1) to triplet (T_1) states via an intermediate triplet (T_2) state. The low reduction potential and ultralong lifetime of the T_1 state facilitate the efficient generation of $O_2^{-\bullet}$ by inter-molecular charge transfer to molecular oxygen. The energy gap of T_1-S_0 is smaller than that between $^3O_2$ and $^1O_2$ thereby precluding the generation of singlet oxygen by the Type-II process. The trimer exhibits superior PDT performance under the hypoxic environment.*

Introduction

Photodynamic therapy (PDT) has attracted significantly increasing attention in the treatment of various cancer diseases over the past decades because of its minimal invasion, low systemic toxicity, negligible drug resistance, and high spatiotemporal selectivity.[1–7] PDT usually involves exposing photosensitizers (PSs) to specific-wavelength light in conjunction with molecular oxygen to generate reactive oxygen species (ROS), which cause tumor cell apoptosis and/or necrosis.[8–12] ROS are dominantly generated from oxygen through two distinct mechanisms called Type-I and Type-II.[13,14] First, photoirradiation excites PSs to a specific excited singlet state (^{1}PS*) which is followed by efficient intersystem crossing (ISC) to an excited triplet state (^{3}PS*).[15,16] In the Type-I process, a cascade of electron and/or proton transfers among ^{3}PS*, adjacent substrates and molecular oxygen produce superoxide ($O_2^{-\bullet}$), peroxide (O_2^{2-}), hydroxyl ($OH^\bullet$) radicals or others; while, in the Type-II process, singlet oxygen ($^1O_2$) is produced by triplet-triplet energy transfer between ^{3}PS* and oxygen.[17]

Up to now, most PSs produce $^1O_2$ by the Type-II process. However, the hypoxic microenvironment of solid tumor ($pO_2 < 5$ mmHg) severely reduces the therapeutic effect of Type-II PSs in PDT because such treatment is heavily dependent on O_2 concentration.[18–21] This has been recognized as a major bottleneck of PDT in the clinical transformation.[22] Unfortunately, rapid O_2 consumption and vascular damage during the type-II PDT further worsen its shortage.[23–25] It is reported that Type-I PSs can lower oxygen dependence by avoiding direct and fast O_2 depletion in PDT to solve the hypoxic problem.[26–29] More importantly, formed $O_2^{-\bullet}$ species by the Type-I process not only serve as oxidants to kill tumor cells, but also participate in superoxide dismutase-triggered catalytic cascades to form highly cytotoxic $OH^\bullet$ species and simultaneously produce O_2 for recycling.[30]

However, to our best knowledge, only one selective Type-I organic photosensitizer has been reported by Peng et al., with emphasis on revealing the action mechanism of $O_2^{-\bullet}$ under hypoxia, leaving molecular design of Type-I PSs unexplored.[30] Although a few groups reported some metal complexes capable of producing ROS through the Type-I process, their short-wavelength absorption, complicated metabolism, and dark toxicity severely limit the clinical application.[31,32] Heavy-metal-free PSs have shown great potential in clinical applications. Some organic PSs that can generate ROS through combined Type-I and -II processes were also reported, as enumerated in Table S1, but rapid O_2 consumption by the Type-II process to certain extent reduces the therapeutic effect.[26,33,34] To maximize the PDT efficiency under hypoxic environment, developing organic Type-I PSs is highly desirable albeit it remains a challenge owing to the lack of general design strategy.[35–37] To generalize molecular design principle for pure Type-I PSs, we propose that several requirements should be fulfilled simultaneously. First, there exist efficient ISC processes from initially populated singlet to triplet excited states, usually the T_1 state. Second, the T_1 state should have a long lifetime for subsequent reactions to produce ROS. Third, the T_1 energy should be lower than that required to produce $^1O_2$ by excitation energy transfer so that the Type-II process is inhibited.[38,39] Fourth, an appropriate redox potential is requested to facilitate electron transfer to

[*] K.-X. Teng,[+] L.-Y. Niu, Q.-Z. Yang
Institution Key Laboratory of Radiopharmaceuticals
College of Chemistry, Beijing Normal University
Beijing 100875 (P. R. China)
E-mail: qzyang@bnu.edu.cn
W.-K. Chen,[+] W.-H. Fang, G. Cui
Key Laboratory of Theoretical and Computational Photochemistry,
Ministry of Education, College of Chemistry
Beijing Normal University, Beijing 100875 (P. R. China)
E-mail: ganglong.cui@bnu.edu.cn
[+] These authors contributed equally to this work.
Supporting information and the ORCID identification number(s) for the author(s) of this article can be found under: https://doi.org/10.1002/anie.202106748.

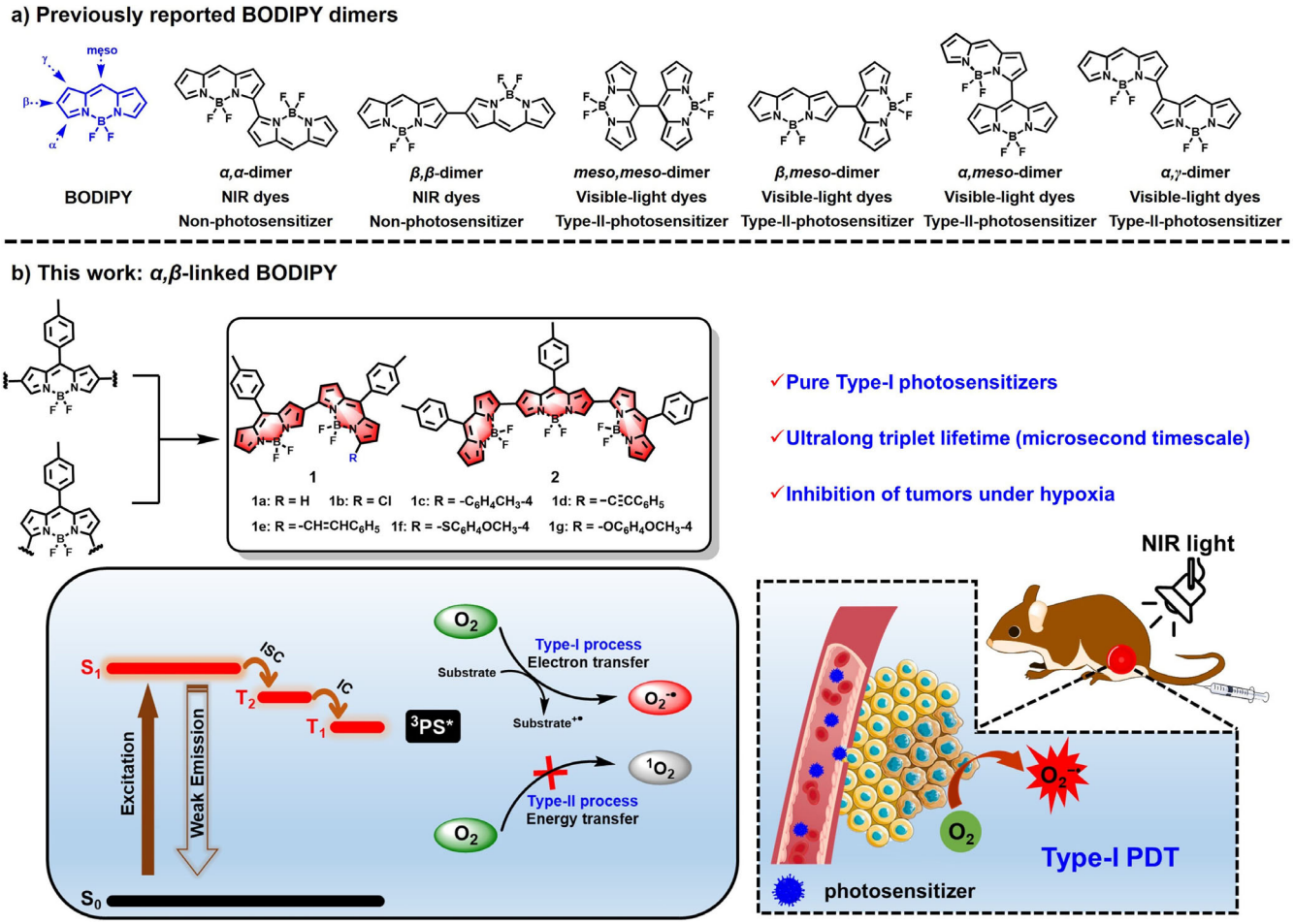

Figure 1. a) Previously reported BODIPY dimers. b) Illustration of structure of α,β-linked BODIPYs and photo-induced exclusive generation of $O_2^{-\bullet}$ radical over $^1O_2$.

yield $O_2^{-\bullet}$. Because of these demanding conditions, the Type-I metal-free PSs have been rarely reported until now.[40]

Herein we report a series of α,β-linked boron dipyrromethene (BODIPY) dimers (**1a–g**) and a trimer (**2**), which generate $O_2^{-\bullet}$ exclusively by the Type-I process upon near-infrared light irradiation (Figure 1b). The efficient triplet formation originates from the initially populated singlet (S_1) to triplet (T_1) states mediated by an intermediate triplet (T_2) state. The ultralong lifetime of the T_1 state up to microsecond timescale and the low reduction potential facilitate efficient $O_2^{-\bullet}$ generation, whereas the low T_1 energy closes the Type-II process down. The T_1-S_0 energy gap of compound **1a** is slightly lower than the energy needed to produce $^1O_2$ by excitation energy transfer (1.05 versus 1.12 eV at CASPT2/PCM level). Compound **2** manifests strong absorption at 740 nm ($\varepsilon = 6.0\times10^4\ M^{-1}\,cm^{-1}$) and ultralong triplet lifetime (1060 μs). It exhibits superior PDT performance under the hypoxic environment of tumor cells. It shows excellent photocytotoxicity in HepG2 cells (2% O_2) with a half-maximal inhibitory concentration (IC_{50}) of 0.56 μM. Note that it is 23-folds lower than the commercial PS **Ce6** at identical conditions. The distinct solid tumor ablation in vivo was also achieved when compound **2** was applied for PDT in tumor treatment of mouse models.

BODIPY derivatives, as sister compounds of porphyrin, have gained considerable attention as PSs in PDT since they possess ideal photosensitizer characteristics: high extinction coefficients, environmental insensitivity, as well as excellent photostability and biocompatibility.[41–45] BODIPY-based PSs are considered most likely to be approved for clinical trials.[46] They are commonly obtained by the introduction of heavy atoms (e.g. transition metals or halogens) into structures to enhance singlet-to-triplet ISC efficiency as a result of heavy-atom effects.[47–50] However, introducing heavy atoms often brings unavoidable disadvantages, such as increased "dark toxicity" and cost, decreased photostability and solubility, as well as reduced triplet-state lifetime.[28,51] BODIPY dimers as heavy-atom-free PSs have attracted increasing attention since the first report of β,*meso*-BODIPY dimer to produce $^1O_2$.[52,53] To date, α,α-, β,β-, *meso,meso*-, β,*meso*-, α,*meso*- and α,γ-linked BODIPY dimers have been reported (Figure 1a).[54–59] Generally, the co-planar BODIPY dimers, that is, α,α- and β,β-dimer, manifest absorption and emission in near-infrared region (NIR), but cannot generate ROS. Orthogonal BODIPY dimers, such as *meso,meso*-, β,*meso*-, α,*meso*- and α,γ-dimer, are used as heavy-atom-free PSs to generate $^1O_2$.[60] However, these BODIPY dimers as potential PSs suffer from two drawbacks: 1) none of them operate in NIR due to the

nonplanar structure, which limits their clinical applications and 2) all of them generate ROS through the Type-II process and their therapeutic effects are thus severely restricted by hypoxia. In this work, α,β-linked BODIPYs exhibit strong absorption in NIR. As pure Type-I PSs, they exclusively generate $O_2^{-\bullet}$ over $^1O_2$, which maintains high PDT efficiency in hypoxic tumors. To our best knowledge, this is the first example of α,β-linked BODIPYs and the first case of BODIPY-based PSs that generate ROS exclusively by the Type-I process.

Results and Discussion

Based on the properties of reported BODIPY dimers, we speculate that α,β-linked BODIPYs would possess excellent photophysical properties as potential PSs for PDT.[61–63] First, α,β-linked BODIPYs with much smaller steric hindrance between two BODIPY units than that of orthogonal dimers could allow the conjugation of two BODIPY units to make absorption red-shifted. Second, electron-deficient α site connected with electron-rich β site might tune electron interaction between the two BODIPY moieties to increase the ISC efficiency and to tune the reduction potential. Keeping this idea in mind, we have designed and synthesized a series of α,β-linked BODIPY dimers and a trimer (Scheme S1). Compound **S2** was obtained from the reaction of **S1** with N-Bromosuccinimide (NBS) at room temperature. Target molecule **1a** was obtained by Suzuki–Miyaura cross-coupling of **S4** with **S3**, which was synthesized through Pd-catalyzed borylation of compound **S2** with bis(pinacolato)diboron (B_2pin_2). To further expand the conjugation, compound **2** was synthesized from **S6** through borylation and Suzuki–Miyaura cross-coupling with **S4**. Compound **3** was obtained through 1,3,5,7-methyl-substituted BODIPY by similar synthetic routes. Compound **1b** was prepared by the same method and it was easily modified to obtain different α,β-linked BODIPY dimers through a one-step coupling reaction or substitution reaction. All new compounds were fully characterized by ^{1}H-NMR, ^{13}C-NMR and high-resolution mass spectrometry (HRMS). Furthermore, crystallography analysis of single crystals of **1a** and **3**, grown from a mixed solvent of n-hexane and dichloromethane, further confirms their molecular structures (Figure 2c and d).

We first chose the simple α,β-linked BODIPY dimer **1a** to study its photophysical properties. As shown in Figure 2e, compound **1a** exhibits intense absorption at 628 nm ($\varepsilon = 4.7 \times 10^4\ M^{-1}cm^{-1}$) and very weak fluorescence at 746 nm ($\Phi_{PL} = 0.8\%$). The optical spectra of **1a** shows a significant bathochromic shift compared with that of BODIPY monomer **S1** and compound **3** with steric hindrance groups. As shown in Figure 2c, crystallography analysis of single-crystal structure indicates that compound **1a** shows planar structure with small dihedral angle of 19.70° for the two BODIPY units (Figure 2c). By contrast, compound **3** exhibits nonplanar conformation with a large dihedral angel of 56.42° in its crystal structure due to the steric hindrance groups (Figure 2d). Therefore, the red-shifted spectra of **1a** is attributed to the expanded π-conjugation.

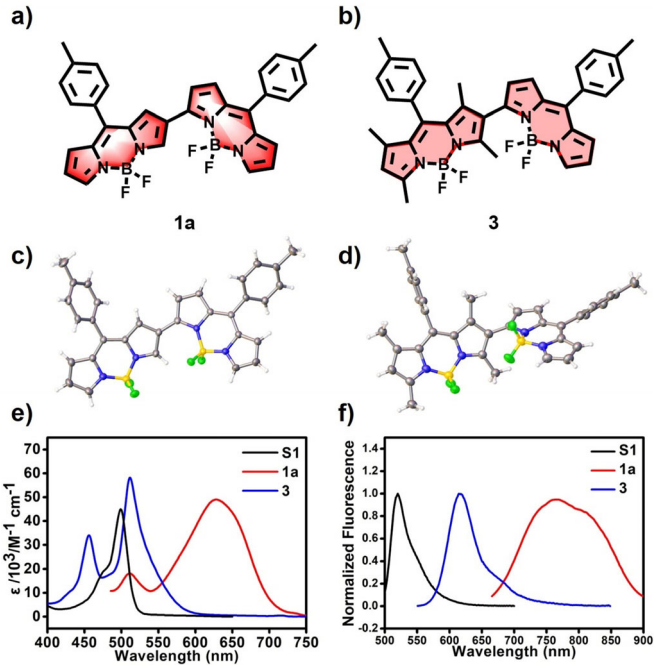

Figure 2. Structures of a) **1a** and b) **3**. Single-crystal structures of c) **1a** and d) **3**. Structures with ellipsoids at 50% probability level. e) Absorption and f) fluorescence spectra of compound **S1**, **1a** and **3** in DMSO (compound was **S1** excited at 500 nm; compound **1a** was excited at 628 nm; compound **3** was excited at 532 nm).

The low fluorescence quantum yield of compound **1a** gives a hint that the ISC process from singlet to triplet excited states might be efficient (Table S3 and Figure S4). To verify this point, we have checked the triplet-state formation through evaluating the ROS generation of compound **1a** by 2′,7′-dichlorodihydrofluorescein (DCFH), a commercial indicator for any general types of ROS. As shown in Figure 3a, the solution of DCFH in the presence of **1a** shows about 65-fold fluorescence enhancement at 522 nm upon light-irradiation (400–800 nm white LED light, 20 mW cm^{-2}) for 3 minutes (Figure S5), indicating the efficient generation of ROS. The fluorescence intensity for **3** does not increase at the identical condition thereby indicating no ROS generation. Then, 9,10-anthracenediyl-bis(methylene)-dimalonic acid (ABDA) as a singlet oxygen scavenger was used to detect $^1O_2$. When ABDA solution in the presence of **1a** was exposed to light-irradiation for 6 minutes, the absorbance of ABDA changes negligibly (Figure S6), indicating no $^1O_2$ generated. We have further detected the $O_2^{-\bullet}$ production by the $O_2^{-\bullet}$ indicator dihydrorhodamine 123 (DHR 123). As shown in Figure 3b, obvious fluorescence enhancement of DHR 123 was observed in the presence of **1a** under illumination, indicating the $O_2^{-\bullet}$ generation (Figure S7). Droethidium (DHE) was also employed to detect the $O_2^{-\bullet}$ generation and the same results were obtained (Figure S9). Electron spin resonance (ESR) spectroscopy was employed to further confirm the $O_2^{-\bullet}$ generation by sensitization of **1a** (Figure 3c). 5,5-dimethyl-1-pyrroline-N-oxide (DMPO) was used as a spin-trap agent for $O_2^{-\bullet}$ and 2,2,6,6-tetramethylpiperidine (TEMP) was applied as a spin trapper to identify $^1O_2$. Upon

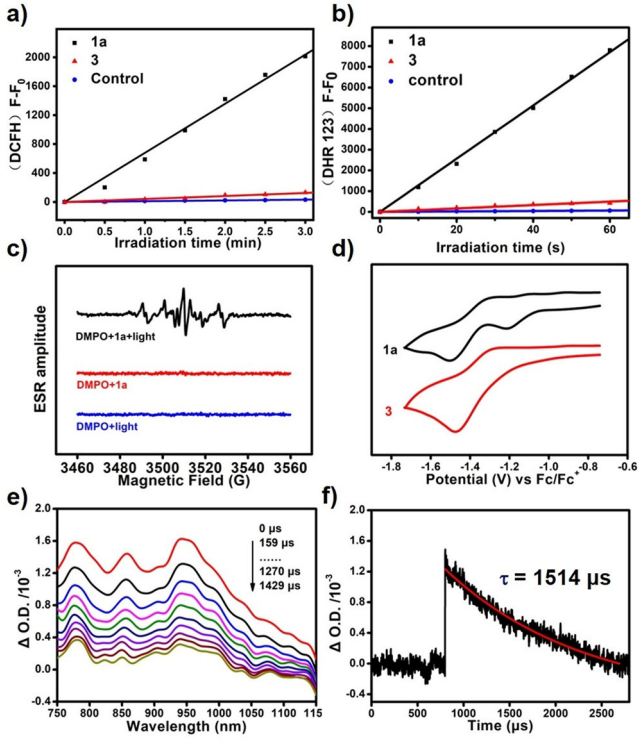

Figure 3. a) ROS and b) $O_2^{-\bullet}$ generation of **1a** and **3**. Both of them were measured in DMSO (10 μM) after irradiation by white LED light source (400–800 nm, 20 mW cm^{-2}). DCFH as a ROS probe (50 μM, $\lambda_{ex}=504$ nm, $\lambda_{em}=522$ nm), DHR123 as a $O_2^{-\bullet}$ probe (60 μM, $\lambda_{ex}=500$ nm, $\lambda_{em}=526$ nm). c) ESR spectra to detect $O_2^{-\bullet}$ generated by **1a** (0.5 mM) under illumination, using DMPO as a spin trapper. d) Cyclic voltammogram of **1a** and **3** in DCM with 0.1 M (n-Bu)$_4$N$^+$PF$_6^-$ as a supporting electrolyte, Ag/Ag$^+$ as a reference electrode, platinum-carbon compound electrode as a working electrode, Pt wire as a counter electrode, and (n-Bu)$_4$N$^+$PF$_6^-$ (0.1 M) as supporting electrolyte, and a scan rate of 20 mV s^{-1}. Fc/Fc$^+$ was used as an external reference. e) Time-resolved transient difference absorption of **1a** in DMSO. f) Decay trace of **1a** at 954 nm.

light-irradiation of the aerated solution of **1a** and DMPO, a characteristic paramagnetic adduct was observed and matched with the $O_2^{-\bullet}$ signal thereby confirming the $O_2^{-\bullet}$ production. No detectable ESR signals was observed when irradiating solution of **1a** and TEMP (Figure S10), which further confirms no generation of $^1O_2$. Based on the above results, we reasonably speculate that **1a** undergoes ISC upon light-irradiation to generate triplet excited states followed by the $O_2^{-\bullet}$ generation through charge transfer.

We further studied electrochemical properties of **1a** to help us understand why **1a** are prone to generating $O_2^{-\bullet}$ via the Type-I process. Cyclic voltammetry was used to investigate redox properties of **1a** and **3**. As shown in Figure 3d, the reduction event of **1a**$^{0/-}$ at −1.21 V (vs. Fc/Fc$^+$) is 260 mV less negative than −1.47 V (vs. Fc/Fc$^+$) that observed for **3**$^{0/-}$. The anodic shifts of **1a** compared to **3** originates from its lower LUMO energy (see Table S6 and Figure S49). The anodic shift of **1a** facilitates it to accept electrons, which endows **1a** with the potential to produce $O_2^{-\bullet}$ by the Type-I process.[16,33,64,65] Another key factor for PSs to generate $O_2^{-\bullet}$ is the lifetime of triplet states. Specifically, the lifetime of triplet states of **1a** is 1514 μs measured by laser flash photolysis (Figures 3e and f). The ultralong lifetime of triplet states is important for electron transfer from substrate to PS thereby improving the $O_2^{-\bullet}$ generation efficiency.

To explore excited-state properties and photophysics of compound **1a**, we carried out theoretical calculations. Ground-state structures were optimized with the B3LYP/6-31G* method while excited-state structures are done with the TD-B3LYP/6-31G* method (see supporting information for computational details).[66–70] Further single-point energies are refined by the much accurate multi-reference complete active space self-consistent field method with second-order perturbation (CASPT2) approach.[71,72] The solvent effects are implicitly considered by the polarizable continuum model (PCM).[73]

The first electronically excited singlet state that is, S_1 is of ππ* character and thus was firstly populated at the Franck-Condon point, that is, the S_0 stable structure, due to relevant considerable transition dipole moments. This singlet state corresponds to exciting an electron from HOMO to LUMO. Because HOMO and LUMO are mostly distributed on the two BODIPY units, the S_1 state is of partial charge-transfer character. Below the bright S_1 state, there are two triplet states available, that is, T_2 and T_1. Both triplet states are of ππ* character, but their electronic characters remain different. The T_1 state is mainly caused by moving an electron from HOMO to LUMO, which is the same as that of the S_1 state. Furthermore, both the S_1 and T_1 states have typical single-reference character. In contrast, the T_2 state is primarily composed of two comparable electronic configurations, that is, HOMO-1 to LUMO and HOMO to LUMO+1 (see Figure 4).

In terms of optimized minima and computed linearly interpolated internal coordinate paths for compound **1a**, an efficient excited-state relaxation pathway from the initially populated S_1 to T_1 states is uncovered as shown in Figure 5a. Upon photoexcitation at the Franck–Condon point, compound **1a** will relax quickly to its S_1 minimum, wherefrom it will further decay to an intermediate T_2 state through an intersystem crossing process. This process is efficient because of a small S_1-T_2 energy gap of 0.13 eV at the S_1 minimum. In

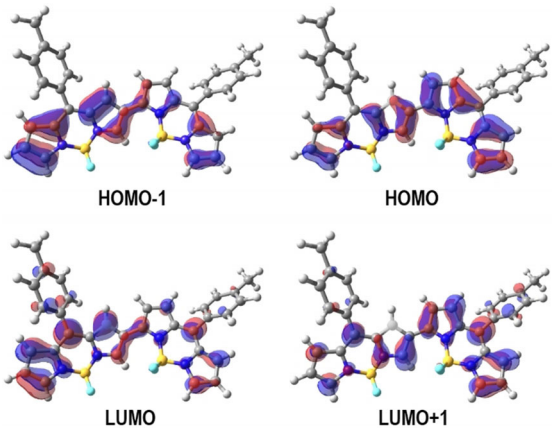

Figure 4. TD-B3LYP/PCM calculated frontier orbitals relevant to the involved excited singlet and triplet states (isosurface value: 0.03).

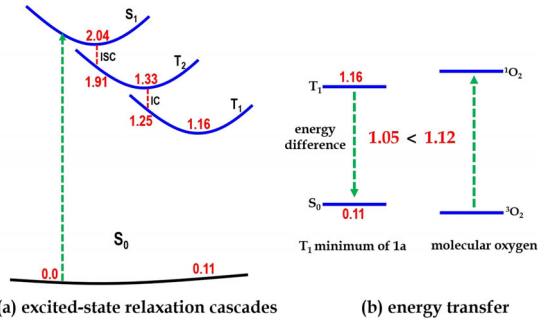

Figure 5. a) Suggested excited-state relaxation pathway from the initially populated S_1 to T_1 states of compound **1a** mediated by an intermediate T_2 state. b) Energy profile for the Type-II energy transfer from the T_1 species of **1a** to $^3O_2$. Also shown are relevant energies (in eV) calculated at the CASPT2/PCM level.

the T_2 state, the system will first relax to its minimum and then continue to decay to the T_1 state followed by a $T_2 \rightarrow T_1$ internal conversion process in the vicinity of the T_2 minimum where the T_2-T_1 energy gap is estimated to be 0.08 eV at the CASPT2/PCM level. In the T_1 state, the system will be trapped for a while because of a very large T_1-S_0 energy gap of 1.05 eV at the CASPT2/PCM level. Moreover, the present calculations demonstrate that excitation energy transfer from the T_1 state of compound **1a** to $^3O_2$ is not favorable in the view of energetics because this process is subtle endothermic. The vertical $T_1 \rightarrow S_0$ emission energy of compound **1a** is calculated at its T_1 minimum to be 1.05 eV at the CASPT2/PCM level, which is a little smaller than that required to excite $^3O_2$ to its singlet excited state producing $^1O_2$ (Figure 5b). The similar situation is also seen for compound **3** (see Figure S50). Therefore, the Type-II process should be not as efficient as the Type-I process observed in the experiments.

To understand the structure-property relationship of α,β-linked BODIPYs, we further designed and synthesized a series of **1a** derivatives with different substituents. Structures of **1a** derivatives are shown in Scheme 1. Their photophysical properties including absorption and fluorescence maxima, molar extinction coefficients (ε) and absolute photoluminescence quantum yields (Φ_{PL}) are summarized in Table 1 (Figures S12–S19). Cyclic voltammetry was used to investigate redox properties of **1b**–**1g** (Figure S20). We have checked their capabilities for $O_2^{-\bullet}$ generation by using DHR 123 as an $O_2^{-\bullet}$ indicator (Figure S21). The results indicate that

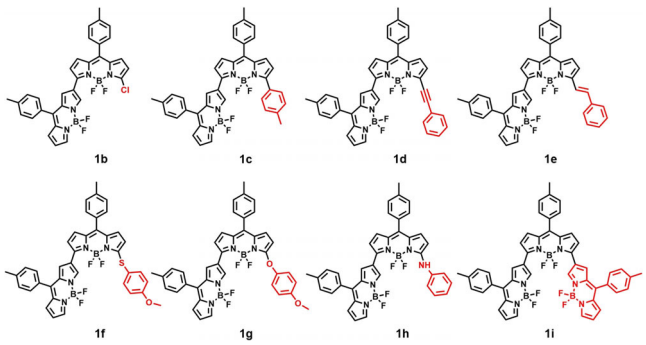

Scheme 1. Structures of compound **1a** derivatives.

Table 1: Photophysical properties of compound **1**.

Compd[a]	λ_{abs} [nm] (ε [$\times 10^{-3}$ $M^{-1}cm^{-1}$][b] Toluene	DCM	DMSO	λ_{PL} [nm][c] Toluene	Φ_{PL} [%][d]
1a	657 (58.3)	628 (46.6)	628 (46.7)	705	7.8
1b	650 (47.0)	630 (45.4)	633 (40.2)	707	5.3
1c	679 (40.6)	665 (39.3)	690 (36.3)	759	3.3
1d	696 (36.3)	676(34.4)	678 (32.5)	752	4.9
1e	683 (30.0)	679 (31.5)	676 (28.9)	782	1.8
1f	677 (30.7)	662 (28.1)	665 (31.3)	770	2.1
1g	651 (34.7)	739 (31.9)	642 (30.1)	748	2.1
1h	640 (53.7)	625 (46.5)	628 (42.8)	676	54.9
1i	742 (22.3)	721 (24.0)	744 (22.2)	818	7.6

[a] 10 μM. [b] Absorption maxima. [c] Fluorescence maxima. [d] Absolute fluorescence quantum yields in toluene.

compound **1b**–**1g** are able to sensitize oxygen to produce $O_2^{-\bullet}$ under light-irradiation. While no $^1O_2$ was detected by utilization of ABDA as a specific indicator for $^1O_2$ for all these BODIPY dimers (Figure S22). We further calculated the T_1-S_0 energy gaps of compounds **1b**, **1c**, **1f** and **1g**, which are also smaller than the $^3O_2$-$^1O_2$ energy difference (Table S7). The reason for no $O_2^{-\bullet}$ generation by **1h** is probably the introduction of amino groups that affect electronic structures. Two large substituents attached on both 3 and 5 positions probably destroyed the quasi-planar structure so that no ROS is generated for **1i**.

To obtain photosensitizers with strong absorption in NIR, we further synthesized α,β-linked BODIPY trimer **2** to expand the conjugation (Figure 6a). Its central BODIPY unit is connected with the two BODIPY groups in β positions and these two groups are far from each other. As expected, compound **2** manifests red-shifted absorption compared with **1a** at 740 nm in DMSO with large molar extinction coefficient of 6.0×10^4 $M^{-1}cm^{-1}$ (Figure 6b). It exhibits weak fluorescence in various solvents (Table S3 and Figure S4). DHR 123, ABDA and DHE were used as indicators for $O_2^{-\bullet}$ and $^1O_2$, respectively, to determine the ability of **2** to generate ROS. The results confirm that **2** exclusively produces $O_2^{-\bullet}$ over $^1O_2$. As shown in Figures 6c and S9, in the presence of compound **2**, the fluorescence of DHR 123 and DHE are significantly enhanced, while the absorption of ABDA changes negligibly under light-irradiation (Figure S8). The ESR experiments further confirm the generation of $O_2^{-\bullet}$ without $^1O_2$ for compound **2** under NIR irradiation (Figures 6d and S10). Furthermore, the laser flash photolysis data show that **2** also possesses an ultra-long triplet state lifetime up to 1060 μs (Figures 6e and f). The above results provide solid evidence that compound **2** is an excellent pure Type-I PS for PDT.

Encouraged by both efficient $O_2^{-\bullet}$ generation and strong absorption ability of compound **2** in near-infrared region with advantages for biological applications, we continue to study its PDT activity in vitro under both normoxic and hypoxic conditions (Figures S23 and S24). The ROS probe, 2′,7′-dichlorodihydrofluorescein diacetate (DCFH-DA), was used to evaluate the cellular ROS during PDT. As shown in Figure 7a, after light-irradiation, bright green fluorescence was observed in **2**-treated HepG2 cells by confocal laser scanning microscopy (CLSM), suggesting effective ROS generation. No $^1O_2$ signal was detected at identical conditions

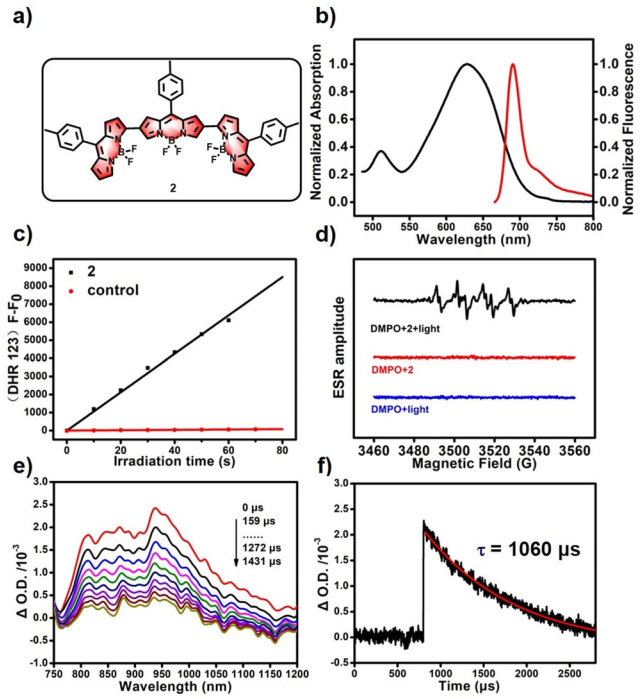

Figure 6. a) Structure of compound **2**. b) Absorption and fluorescence spectra of compound **2** in DMSO. c) The $O_2^{-\bullet}$ generation of **2** (10 μM) in DMSO, using DHR 123 as $O_2^{-\bullet}$ probe (60 μM, $\lambda_{ex}=500$ nm, $\lambda_{em}=526$ nm). d) The ESR spectra to detect $O_2^{-\bullet}$ generated by **2** (0.5 mM) under illumination, using DMPO as spin trapper. e) Time-resolved transient difference absorption of **2** in DMSO. f) Decay trace of **2** at 937 nm.

when singlet oxygen sensor green reagent (SOSG, a commercial $^1O_2$ probe) was employed (iodine-bearing BODIPY as a reference, Figure S25). DHE as a $O_2^{-\bullet}$ probe was employed to evaluate the cellular $O_2^{-\bullet}$ species in normoxic environments (21% O_2) and hypoxic environment (2% O_2). As shown in Figure 7b, bright red fluorescence was detected in **2**-treated HepG2 cells under both normoxic and hypoxic environment after illumination, suggesting **2** could generate $O_2^{-\bullet}$ even under hypoxic environment. Then, we evaluated the PDT effects of **2** to HepG2 cells by cell counting kit-8 (CCK-8) assays. Under irradiation with LED light (730 nm, 50 mW cm^{-2}) for 10 min, compound **2** shows obvious cytotoxicity to HepG2 cells in normoxic environments, with a half-maximal inhibitory concentration (IC_{50}) of 0.39 μM (Figure 7c). More importantly, compound **2** also manifests good anti-tumor effects even under hypoxic conditions with an IC_{50} of 0.56 μM. In the absence of light-irradiation, **2** shows no toxicity to HepG2 cells under both normoxia and hypoxia conditions (Figure 7d). As shown in Figures 7e and f, when commercial PS **Ce6** was exposed to LED light-irradiation (660 nm, 50 mW cm^{-2}), IC_{50} was 6.0 μM under normoxia which is 15.3-fold higher than that of **2**, and it was 12.9 μM under hypoxia, 23.2-fold higher than that of **2**. These results indicate that **2**, as a pure Type-I PS, is less dependent on oxygen concentration, and is still able to generate ROS to inhibit tumor proliferation even under hypoxic conditions.

Next, a calcein-AM and propidium iodide (PI) assay was employed to evaluate the inhibition of tumor cells by **2** with light-irradiation. Viable cells were stained by calcein-AM to emit fluorescence in the green channel and apoptotic cells were stained by PI to emit fluorescence in the red channel. It can be seen in Figure 7g that HepG2 cells treated with 0.16 μM **2** showed obvious fluorescence in the green and red channels after illumination indicating partial cell death. When the **2** concentration increased to 0.64 μM, only the red channel had signal, indicating that all the HepG2 cells were dead. By contrast, the cells without **2** only exhibited fluorescence in the green channel under identical conditions, indicating no cell death. Furthermore, an Annexin V-FITC/PI apoptosis detection kit was used to investigate the possible death mechanism by flow cytometry experiments. The results in Figure 7h demonstrated that the cell toxicity was mainly associated with apoptosis. These results prove that **2** effectively induces tumor cell apoptosis under illumination.

We chose a block copolymer, Pluronic F127, as the encapsulation matrix to co-assemble with **2** to form nanoparticles for therapy in vivo. The nanoparticles were characterized as well-dispersed nanoparticles by dynamic light scattering (DLS) and scanning electron microscope (SEM) (Figure S26). The absorption spectrum, fluorescence spectrum and superoxide anion radical generation of nanoparticles was detected in water to confirm that they can absorb NIR light to generate $O_2^{-\bullet}$ after assembly (Figures S27–S29). The absorbance of nanoparticles showed almost no change after 60 minutes of irradiation (Figure S30), indicating their high photostability. Furthermore, absorption of nanoparticles for a constant 48 h in fetal calf serum, indicated that nanoparticles of compound **2** are remarkably stable under physiological conditions (Figure S30). Then we evaluated the tumor enrichment effect of the nanoparticles on immunodeficient mouse models by subcutaneous tumor model of human liver cancer HepG2 cells in BALB/c mice. As shown in Figure S31, obvious fluorescence was detected in the tumor position after 3 hours for intravenous injection due to the enhanced permeability and retention (EPR) effect.[74] At 24 hours after the injection, the ex vivo biodistribution of the photosensitizer was evaluated (Figure S31c), and the fluorescence in the tumor was stronger than that in other organs. We further investigated the antitumor efficiency of PDT by compound **2** in vivo for HepG-2 tumor-bearing immunocompetent BALB/c mice (primary tumor volume: ≈100 mm^3). The nanoparticles of compound **2** were injected into the mice by tail vein injection, followed by irradiation (730 nm LED light, 120 mW cm^{-2}) at 12 hours and 24 hours post injection. Then, the body weights (Figure 8a) and tumor volumes (Figure 8b) were recorded during the subsequent 12 days. The weight of the mice increased slightly, suggesting the negligible systemic cytotoxicity of **2** during PDT. For the group treated with **2** with light, the tumor of mice disappeared on the sixth day after irradiation and did not relapse, indicating that **2** effectively suppressed the tumor. The group treated with **2** without irradiation exhibited similar tumor growth rate to the PBS-treated group, suggesting that **2** was nontoxic in the absence of light. The mice were sacrificed on the 12th day and all the tumor tissues were peeled and weighed (Figures 8c and d). The hematoxylin & eosin (H&E) staining was applied to examine tumor damage of **2** (Fig-

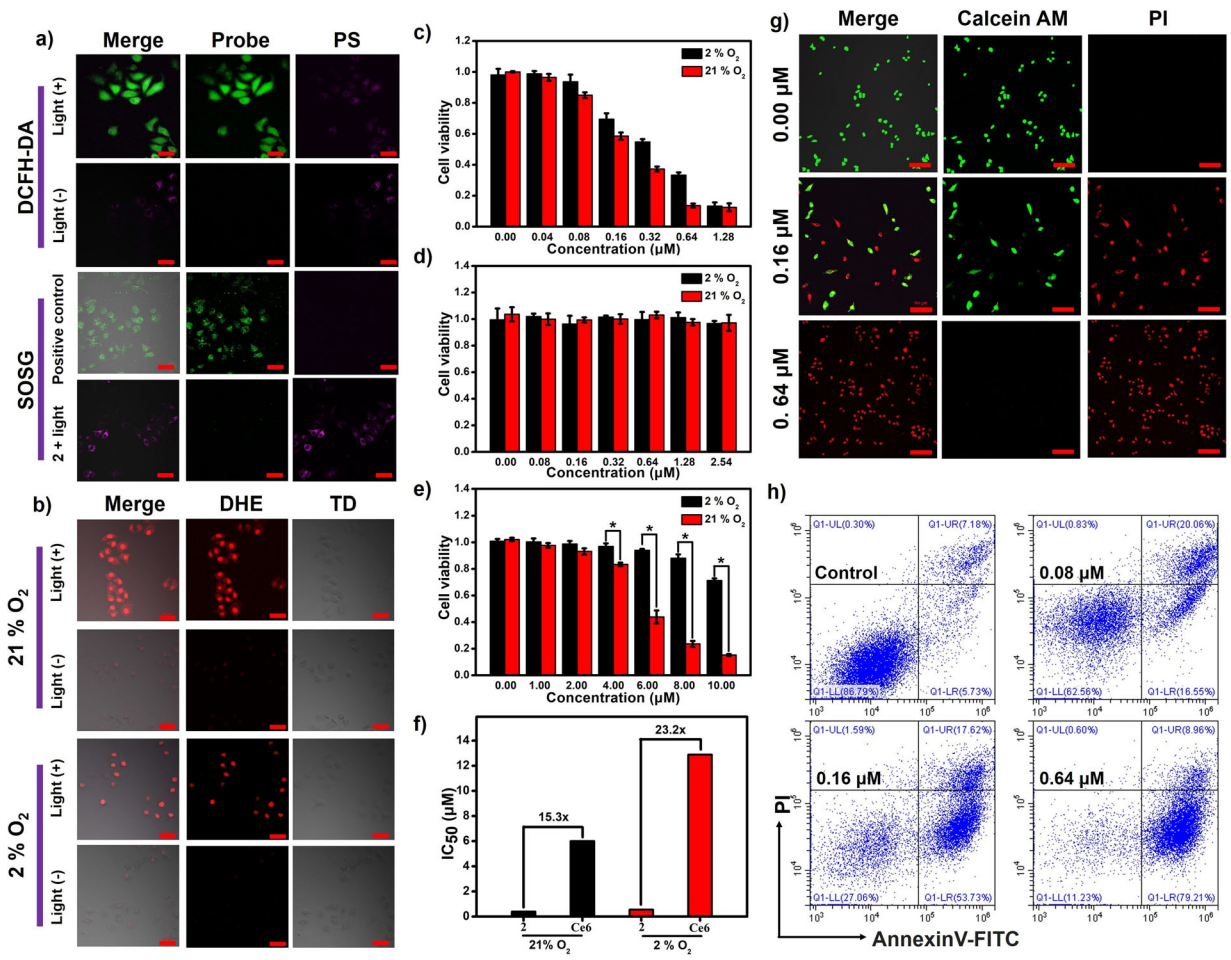

Figure 7. a) Detection of ROS and $^1O_2$ in HepG2 cells with DCFH-DA and SOSG. The scale bar represents 50 μm. b) $O_2^{-\bullet}$ detection in HepG2 cells under normoxia (21 % O_2) and hypoxia (2 % O_2) conditions by using DHE. The scale bar represents 50 μm. Cell viability of HepG2 cells subjected to a range of **2** concentrations in the c) presence and d) absence of light-irradiation under normoxia or hypoxia conditions. e) Cell viability of HepG2 cells subjected to a range of **Ce6** concentration in the presence of light-irradiation under normoxia (21 % O_2) or hypoxia (2 % O_2). $*P<0.05$ (one-way ANOVA) f) The half-maximal inhibitory concentration of **2** and **Ce6** under normoxia and hypoxia. g) CLSM images of calcein AM/PI-stained HepG2 cells. The scale bar represents 100 μm. h) Apoptosis analysis of HepG2 cells treated with **2** at various doses. (the parameter of CLSM: green channel: 500–550 nm, excited at 487 nm; red channel: 570–620 nm, excited at 562 nm; NIR channel: 663–738 nm, excited at 638 nm).

ure S32) and the results showed that **2** could destroy tumor tissue.

Conclusion

In this work we have reported a series of heavy-atom-free superoxide radical species generators based on α,β-linked BODIPYs, which exhibit excellent potential as specific Type-I photosensitizers in PDT. They exclusively produce $O_2^{-\bullet}$ by the Type-I process upon NIR light illumination and have large molar extinction coefficients in NIR, ultra-long triplet lifetimes up to microsecond timescale, low dark toxicity, and great phototoxicity.

The quasi-planar conformational structure of these α,β-linked BODIPYs plays an important role in red-shifted absorption band and lowering their reduction potential. Subsequent theoretical studies on compound **1a** uncovered an efficient excited-state radiationless relaxation pathway from the initially populated S_1 to T_1 states, in which a multi-reference intermediate T_2 state plays as a relay to regulate relevant inter-state nonradiative electronic transitions. It is also found that the inter-molecular energy transfer process from the T_1 state of compound **1a** to O_2 by the Type-II process is precluded due to the energy gap of T_1-S_0 being narrower than that between $^3O_2$ and $^1O_2$. In contrast, the Type-I process that generates superoxide $O_2^{-\bullet}$ radical becomes efficient because of the low reduction potential and the long lived T_1 state up to microsecond. Consequently, these BODIPY-based dimers and trimer solely produce superoxide radical species by the Type-I photosensitization, which coincides with the present experimental measurement.

Furthermore, in vitro studies demonstrate that α,β-linked BODIPY trimer **2** have excellent anti-tumor effects even under environments with severe O_2 shortage, and its PDT effects are evidently superior to that of the commercial **Ce6**. The further in vivo studies reveal that compound **2** shows irreversible cytotoxicity to tumor tissue resulting in distinct

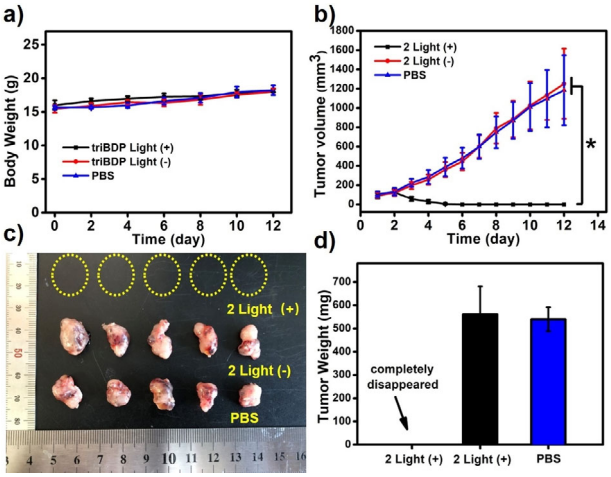

Figure 8. a) Body weights of the mice during the observation. b) Tumor growth profiles during the observation. $^*P<0.05$ (one-way ANOVA). c) Images of tumor tissues from different groups of tumors bearing mice. d) Average tumor weight of different groups of tumor-bearing mice.

solid tumor ablation. These results indicate that these α,β-linked BODIPYs can serve as a novel class of PDT agents for potential application in clinical treatments in due future.

Finally, our work could motivate experimental and theoretical chemists to comprehensively and systematically explore both potential applications and related mechanisms of Type-I photosensitizers in broad fields of photocatalysis, biomaterials, physical chemistry and medicine chemistry. The general design principles proposed in this work could help chemists rationally design various excellent heavy-atom-free PDT photosensitizers for generating ROS exclusively by the Type-I mechanism.

Acknowledgements

We are grateful for financial support from the National Natural Science Foundation of China (21971023, 21525206, and 21688102). We thank Yanhong Liu at Technical Institute of Physics and Chemistry, CAS for assistance with ESR studies and Heng Lu at Technical Institute of Physics and Chemistry, CAS for assistance with laser flash photolysis test.

Conflict of Interest

The authors declare no conflict of interest.

Keywords: BODIPY · hypoxia · photodynamic therapy · photosensitizers · superoxide radical

[1] T. J. Dougherty, C. J. Gomer, B. W. Henderson, G. Jori, D. Kessel, M. Korbelik, J. Moan, Q. Peng, *J. Natl. Cancer Inst.* **1998**, *90*, 889 – 905.
[2] D. E. J. G. J. Dolmans, D. Fukumura, R. K. Jain, *Nat. Rev. Cancer* **2003**, *3*, 380 – 387.
[3] L. B. Josefsen, R. W. Boyle, *Met.-Based Drugs* **2008**, *2008*, 276109 – 276109.
[4] B. M. Luby, C. D. Walsh, G. Zheng, *Angew. Chem. Int. Ed.* **2019**, *58*, 2558 – 2569; *Angew. Chem.* **2019**, *131*, 2580 – 2591.
[5] P. Agostinis, K. Berg, K. A. Cengel, T. H. Foster, A. W. Girotti, S. O. Gollnick, S. M. Hahn, M. R. Hamblin, A. Juzeniene, D. Kessel, M. Korbelik, J. Moan, P. Mroz, D. Nowis, J. Piette, B. C. Wilson, J. Golab, *CA-Cancer J. Clin.* **2011**, *61*, 250 – 281.
[6] X. Zhao, J. Liu, J. Fan, H. Chao, X. Peng, *Chem. Soc. Rev.* **2021**, *50*, 4185 – 4219.
[7] J. M. Dąbrowski, L. G. Arnaut, *Photochem. Photobiol. Sci.* **2015**, *14*, 1765 – 1780.
[8] A. P. Castano, T. N. Demidova, M. R. Hamblin, *Photodiagn. Photodyn. Ther.* **2005**, *2*, 1 – 23.
[9] A. P. Castano, P. Mroz, M. R. Hamblin, *Nat. Rev. Cancer* **2006**, *6*, 535 – 545.
[10] H. Huang, B. Yu, P. Zhang, J. Huang, Y. Chen, G. Gasser, L. Ji, H. Chao, *Angew. Chem. Int. Ed.* **2015**, *54*, 14049 – 14052; *Angew. Chem.* **2015**, *127*, 14255 – 14258.
[11] W. Fan, P. Huang, X. Chen, *Chem. Soc. Rev.* **2016**, *45*, 6488 – 6519.
[12] S. Li, Q. Zou, Y. Li, C. Yuan, R. Xing, X. Yan, *J. Am. Chem. Soc.* **2018**, *140*, 10794 – 10802.
[13] Z. Zhou, J. Song, L. Nie, X. Chen, *Chem. Soc. Rev.* **2016**, *45*, 6597 – 6626.
[14] X. Li, S. Lee, J. Yoon, *Chem. Soc. Rev.* **2018**, *47*, 1174 – 1188.
[15] X. Li, N. Kwon, T. Guo, Z. Liu, J. Yoon, *Angew. Chem. Int. Ed.* **2018**, *57*, 11522 – 11531; *Angew. Chem.* **2018**, *130*, 11694 – 11704.
[16] Z. Zhuang, J. Dai, M. Yu, J. Li, P. Shen, R. Hu, X. Lou, Z. Zhao, B. Z. Tang, *Chem. Sci.* **2020**, *11*, 3405 – 3417.
[17] B. Yuan, H. Wu, H. Wang, B. Tang, J.-F. Xu, X. Zhang, *Angew. Chem. Int. Ed.* **2021**, *60*, 706 – 710; *Angew. Chem.* **2021**, *133*, 716 – 720.
[18] Q. Chen, L. Feng, J. Liu, W. Zhu, Z. Dong, Y. Wu, Z. Liu, *Adv. Mater.* **2016**, *28*, 7129 – 7136.
[19] W. Piao, K. Hanaoka, T. Fujisawa, S. Takeuchi, T. Komatsu, T. Ueno, T. Terai, T. Tahara, T. Nagano, Y. Urano, *J. Am. Chem. Soc.* **2017**, *139*, 13713 – 13719.
[20] J. Du, T. Shi, S. Long, P. Chen, W. Sun, J. Fan, X. Peng, *Coord. Chem. Rev.* **2021**, *427*, 213604.
[21] Z. Liu, T. Cao, Y. Xue, M. Li, M. Wu, J. W. Engle, Q. He, W. Cai, M. Lan, W. Zhang, *Angew. Chem. Int. Ed.* **2020**, *59*, 3711 – 3717; *Angew. Chem.* **2020**, *132*, 3740 – 3746.
[22] Detection and Characterization of Tumor Hypoxia Using pO_2 Histography, P. Vaupel, M. Höckel, A. Mayer, *Antioxid. Redox Signaling* **2007**, *9*, 1221 – 1235.
[23] W. Yu, T. Liu, M. Zhang, Z. Wang, J. Ye, C.-X. Li, W. Liu, R. Li, J. Feng, X.-Z. Zhang, *ACS Nano* **2019**, *13*, 1784 – 1794.
[24] M. Li, T. Xiong, J. Du, R. Tian, M. Xiao, L. Guo, S. Long, J. Fan, W. Sun, K. Shao, X. Song, J. W. Foley, X. Peng, *J. Am. Chem. Soc.* **2019**, *141*, 2695 – 2702.
[25] M. Li, Y. Shao, J. H. Kim, Z. Pu, X. Zhao, H. Huang, T. Xiong, Y. Kang, G. Li, K. Shao, J. Fan, J. W. Foley, J. S. Kim, X. Peng, *J. Am. Chem. Soc.* **2020**, *142*, 5380 – 5388.
[26] Y.-Y. Wang, Y.-C. Liu, H. Sun, D.-S. Guo, *Coord. Chem. Rev.* **2019**, *395*, 46 – 62.
[27] J. Sun, K. Du, J. Diao, X. Cai, F. Feng, S. Wang, *Angew. Chem. Int. Ed.* **2020**, *59*, 12122 – 12128; *Angew. Chem.* **2020**, *132*, 12220 – 12226.
[28] J. Dai, Y. Li, Z. Long, R. Jiang, Z. Zhuang, Z. Wang, Z. Zhao, X. Lou, F. Xia, B. Z. Tang, *ACS Nano* **2020**, *14*, 854 – 866.
[29] V.-N. Nguyen, Y. Yan, J. Zhao, J. Yoon, *Acc. Chem. Res.* **2021**, *54*, 207 – 220.
[30] M. Li, J. Xia, R. Tian, J. Wang, J. Fan, J. Du, S. Long, X. Song, J. W. Foley, X. Peng, *J. Am. Chem. Soc.* **2018**, *140*, 14851 – 14859.
[31] I. Ashur, R. Goldschmidt, I. Pinkas, Y. Salomon, G. Szewczyk, T. Sarna, A. Scherz, *J. Phys. Chem. A* **2009**, *113*, 8027 – 8037.

[32] T. Luo, K. Ni, A. Culbert, G. Lan, Z. Li, X. Jiang, M. Kaufmann, W. Lin, *J. Am. Chem. Soc.* **2020**, *142*, 7334 – 7339.
[33] K. Plaetzer, B. Krammer, J. Berlanda, F. Berr, T. Kiesslich, *Lasers Med. Sci.* **2009**, *24*, 259 – 268.
[34] A. Roxin, J. Chen, A. S. Paton, T. P. Bender, G. Zheng, *J. Med. Chem.* **2014**, *57*, 223 – 237.
[35] Q. Li, C. Huang, L. Liu, R. Hu, J. Qu, *Cytometry Part A* **2018**, *93*, 997 – 1003.
[36] L. Li, C. Shao, T. Liu, Z. Chao, H. Chen, F. Xiao, H. He, Z. Wei, Y. Zhu, H. Wang, X. Zhang, Y. Wen, B. Yang, F. He, L. Tian, *Adv. Mater.* **2020**, *32*, 2003471.
[37] J. Sun, X. Cai, C. Wang, K. Du, W. Chen, F. Feng, S. Wang, *J. Am. Chem. Soc.* **2021**, *143*, 868 – 878.
[38] M. C. DeRosa, R. J. Crutchley, *Coord. Chem. Rev.* **2002**, *233*, 351 – 371.
[39] J. Zhao, K. Xu, W. Yang, Z. Wang, F. Zhong, *Chem. Soc. Rev.* **2015**, *44*, 8904 – 8939.
[40] X. Cui, G. Lu, S. Dong, S. Li, Y. Xiao, J. Zhang, Y. Liu, X. Meng, F. Li, C.-S. Lee, *Mater. Horiz.* **2021**, *8*, 571 – 576.
[41] G. Ulrich, R. Ziessel, A. Harriman, *Angew. Chem. Int. Ed.* **2008**, *47*, 1184 – 1201; *Angew. Chem.* **2008**, *120*, 1202 – 1219.
[42] L.-Y. Niu, Y.-S. Guan, Y.-Z. Chen, L.-Z. Wu, C.-H. Tung, Q.-Z. Yang, *J. Am. Chem. Soc.* **2012**, *134*, 18928 – 18931.
[43] A. Kamkaew, S. H. Lim, H. B. Lee, L. V. Kiew, L. Y. Chung, K. Burgess, *Chem. Soc. Rev.* **2013**, *42*, 77 – 88.
[44] S. Ye, J. Rao, S. Qiu, J. Zhao, H. He, Z. Yan, T. Yang, Y. Deng, H. Ke, H. Yang, Y. Zhao, Z. Guo, H. Chen, *Adv. Mater.* **2018**, *30*, 1801216.
[45] A. Turksoy, D. Yildiz, E. U. Akkaya, *Coord. Chem. Rev.* **2019**, *379*, 47 – 64.
[46] J. Wang, Q. Gong, L. Wang, E. Hao, L. Jiao, *J. Porphyrins Phthalocyanines* **2020**, *24*, 603 – 635.
[47] A. Gorman, J. Killoran, C. O'Shea, T. Kenna, W. M. Gallagher, D. F. O'Shea, *J. Am. Chem. Soc.* **2004**, *126*, 10619 – 10631.
[48] J. Zhao, W. Wu, J. Sun, S. Guo, *Chem. Soc. Rev.* **2013**, *42*, 5323 – 5351.
[49] R. Wang, K. Dong, G. Xu, B. Shi, T. Zhu, P. Shi, Z. Guo, W.-H. Zhu, C. Zhao, *Chem. Sci.* **2019**, *10*, 2785 – 2790.
[50] K.-X. Teng, L.-Y. Niu, Y.-F. Kang, Q.-Z. Yang, *Chem. Sci.* **2020**, *11*, 9703 – 9711.
[51] S. Qi, N. Kwon, Y. Yim, V.-N. Nguyen, J. Yoon, *Chem. Sci.* **2020**, *11*, 6479 – 6484.
[52] Y. Cakmak, S. Kolemen, S. Duman, Y. Dede, Y. Dolen, B. Kilic, Z. Kostereli, L. T. Yildirim, A. L. Dogan, D. Guc, E. U. Akkaya, *Angew. Chem. Int. Ed.* **2011**, *50*, 11937 – 11941; *Angew. Chem.* **2011**, *123*, 12143 – 12147.
[53] S. Duman, Y. Cakmak, S. Kolemen, E. U. Akkaya, Y. Dede, *J. Org. Chem.* **2012**, *77*, 4516 – 4527.
[54] M. Bröring, R. Krüger, S. Link, C. Kleeberg, S. Köhler, X. Xie, B. Ventura, L. Flamigni, *Chem. Eur. J.* **2008**, *14*, 2976 – 2983.
[55] Y. Liu, J. Zhao, A. Iagatti, L. Bussotti, P. Foggi, E. Castellucci, M. Di Donato, K.-L. Han, *J. Phys. Chem. C* **2018**, *122*, 2502 – 2511.
[56] A. B. Nepomnyashchii, M. Bröring, J. Ahrens, A. J. Bard, *J. Am. Chem. Soc.* **2011**, *133*, 19498 – 19504.
[57] Y. Hayashi, S. Yamaguchi, W. Y. Cha, D. Kim, H. Shinokubo, *Org. Lett.* **2011**, *13*, 2992 – 2995.
[58] M. T. Whited, N. M. Patel, S. T. Roberts, K. Allen, P. I. Djurovich, S. E. Bradforth, M. E. Thompson, *Chem. Commun.* **2012**, *48*, 284 – 286.
[59] D. Wang, Q. Wu, X. Zhang, W. Wang, E. Hao, L. Jiao, *Org. Lett.* **2020**, *22*, 7694 – 7698.
[60] M. A. Filatov, *Org. Biomol. Chem.* **2020**, *18*, 10 – 27.
[61] Y. Dong, A. A. Sukhanov, J. Zhao, A. Elmali, X. Li, B. Dick, A. Karatay, V. K. Voronkova, *J. Phys. Chem. C* **2019**, *123*, 22793 – 22811.
[62] J. T. Buck, A. M. Boudreau, A. DeCarmine, R. W. Wilson, J. Hampsey, T. Mani, *Chem* **2019**, *5*, 138 – 155.
[63] Z. Wang, M. Ivanov, Y. Gao, L. Bussotti, P. Foggi, H. Zhang, N. Russo, B. Dick, J. Zhao, M. Di Donato, G. Mazzone, L. Luo, M. Fedin, *Chem. Eur. J.* **2020**, *26*, 1091 – 1102.
[64] J. Davila, A. Harriman, *Photochem. Photobiol.* **1989**, *50*, 29 – 35.
[65] H. Huang, S. Banerjee, K. Qiu, P. Zhang, O. Blacque, T. Malcomson, M. J. Paterson, G. J. Clarkson, M. Staniforth, V. G. Stavros, G. Gasser, H. Chao, P. J. Sadler, *Nat. Chem.* **2019**, *11*, 1041 – 1048.
[66] A. D. Becke, *Phys. Rev. A* **1988**, *38*, 3098 – 3100.
[67] C. Lee, W. Yang, R. G. Parr, *Phys. Rev. B* **1988**, *37*, 785.
[68] S. H. Vosko, L. Wilk, M. Nusair, *J. Phys.* **1980**, *58*, 1200 – 1211.
[69] A. D. Becke, *J. Chem. Phys.* **1993**, *98*, 1372 – 1377.
[70] M. Marques, A. Rubio, E. K. Gross, K. Burke, F. Nogueira, C. A. Ullrich, *Time-dependent density functional theory. Lecture notes in physics*, vol 706, Springer Science & Business Media, Cham, **2006**, https://doi.org/10.1007/b11767107.
[71] K. Andersson, P. A. Malmqvist, B. O. Roos, A. J. Sadlej, K. Wolinski, *J. Phys. Chem.* **1990**, *94*, 5483 – 5488.
[72] K. Andersson, P.-Å. Malmqvist, B. O. Roos, *J. Phys. Chem.* **1992**, *96*, 1218 – 1226.
[73] V. Barone, M. Cossi, *J. Phys. Chem. A* **1998**, *102*, 1995 – 2001.
[74] I. de Lázaro, D. J. Mooney, *Nat. Mater.* **2020**, *19*, 486 – 487.

Manuscript received: May 19, 2021
Revised manuscript received: June 20, 2021
Accepted manuscript online: July 6, 2021
Version of record online: ■■ ■■, ■■■■

Research Articles

Photodynamic Therapy

K.-X. Teng, W.-K. Chen, L.-Y. Niu, W.-H. Fang, G. Cui,* Q.-Z. Yang* _____ ■■■■–■■■■

BODIPY-Based Photodynamic Agents for Exclusively Generating Superoxide Radical over Singlet Oxygen

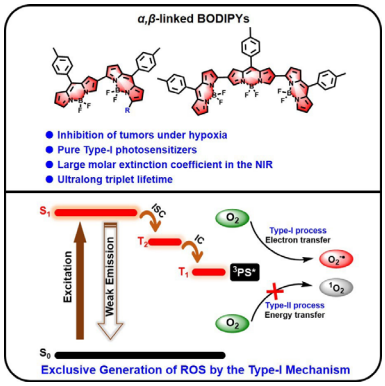

Heavy-atom-free boron dipyrromethene (BODIPY)-based photosensitizers generate ROS exclusively by the Type-I process upon near-infrared light illumination for tumor ablation.